Available online at www.sciencedirect.com

ScienceDirect

Advances in Space Research 67 (2021) 35–45

ADVANCES IN SPACE RESEARCH (a COSPAR publication)

www.elsevier.com/locate/asr

Can an impulsive variation of the solar wind plasma pressure trigger a plasma bubble? A case study based on CSES, Swarm and THEMIS data

M. Piersanti [a], M. Pezzopane [b,*], Z. Zhima [c,d], P. Diego [e], C. Xiong [f], R. Tozzi [b], A. Pignalberi [b], G. D'Angelo [e], R. Battiston [g], J. Huang [d], P. Picozza [a], Y. Rui [c,d], X. Shen [c,d], R. Sparvoli [h], P. Ubertini [e], Y. Yang [c,d], S. Zoffoli [i]

[a] *INFN – University of Rome "Tor Vergata", Rome, Italy*
[b] *Istituto Nazionale di Geofisica e Vulcanologia, Rome, Italy*
[c] *Institute of Earthquake Forecasting, China Earthquake Administration, Beijing, China*
[d] *Institute of Crustal Dynamics, China Earthquake Administration, Beijing, China*
[e] *INAF-Istituto di Astrofisica e Planetologia Spaziali, Rome, Italy*
[f] *GFZ German Research Centre for Geosciences, Potsdam, Germany*
[g] *TIFPA and University of Trento, Trento, Italy*
[h] *University of Rome "Tor Vergata", Rome, Italy*
[i] *Agenzia Spaziale Italiana, Rome, Italy*

Received 19 June 2020; received in revised form 18 July 2020; accepted 29 July 2020
Available online 13 August 2020

Abstract

During the August 25, 2018 geomagnetic storm, the new borne CSES-01 satellite and the Swarm A satellite detected a really large equatorial plasma bubble (EPB) in the post-midnight sector over western Africa. We investigated the features of this deep ionospheric plasma depletion using data from the Langmuir probes on-board CSES-01 and Swarm A satellites, and data from the high-precision magnetometer and the electric field detector instruments on-board CSES-01. Using also plasma and magnetic field data from THEMIS-E satellite we found that, during the passage of the magnetic cloud that drove the geomagnetic storm, an impulsive variation lasting about ten minutes characterized the solar wind (SW) pressure. The analysis of the delay time, between the occurrence of such impulsive variation and the detection of the plasma bubble, suggests a possible link between the SW pressure impulsive variation as identified by THEMIS-E and the generation of the EPB as detected by CSES-01 and Swarm A. We put forward the hypothesis that the SW pressure impulsive variation might have triggered an eastward prompt penetrating electric field that propagated from high to equatorial latitudes, overlapping in the nightside region to the zonal westward electric field, causing either a reduction or an inversion, at the base of the EPB triggering.

Keywords: Equatorial plasma bubble; Solar wind-magnetosphere-ionosphere coupling; Geomagnetic storm; CSES; Swarm; THEMIS

* Corresponding author.
E-mail addresses: mirko.piersanti@roma2.infn.it (M. Piersanti), michael.pezzopane@ingv.it (M. Pezzopane), piero.diego@inaf.it (P. Diego), bear@gfz-potsdam.de (C. Xiong), roberta.tozzi@ingv.it (R. Tozzi), roberto.battiston@unitn.it (R. Battiston), picozza@roma2.infn.it (P. Picozza), shenxuhui@vip.sina.com (X. Shen), roberta.sparvoli@roma2.infn.it (R. Sparvoli), pietro.ubertini@inaf.it (P. Ubertini), simona.zoffoli@asi.it (S. Zoffoli).

1. Introduction

Plasma density depletions, which are observed in the equatorial ionosphere at different spatial (~50–1000 km) and temporal scales, are called equatorial plasma bubbles (EPBs). Typically, EPBs are detected within a narrow band

https://doi.org/10.1016/j.asr.2020.07.046
0273-1177/

of ±20° dip latitude, at altitudes between the bottomside of the ionospheric F region and up to ~1000 km of altitude (Woodman and Hoz, 1976; Ossakow and Chaturvedi, 1978). Tsunoda (1980) and Tsunoda et al. (1982) showed that EPBs appear primarily at local dusk and, during their ascending motion in the ionosphere, present a stretched, wedge-like structure in the north–south direction along the geomagnetic field lines. As a matter of fact, after local sunset, at low latitudes the so-called pre-reversal enhancement of the equatorial anomaly (Woodman, 1970) generates an upward plasma drift (due to a steep vertical electron density gradient caused by the E-layer disappearance) and, if the Rayleigh-Taylor instability growth rate is large enough, plasma irregularities and depletions can be generated (Farley et al., 1970; Retterer and Roddy, 2014).

When a geomagnetic storm occurs, electric field perturbations can be generated by prompt penetration electric fields (PPEFs) of magnetospheric origin and/or by the so-called ionospheric disturbance dynamo (e.g. Blanc and Richmond, 1980; Fejer and Scherliess, 1995; Fejer et al., 2008; Huang et al., 2007a, 2007b; Piersanti et al., 2017). On the dusk sector, PPEFs can superimpose on the background low-latitude zonal electric field that is present also under quiet conditions. This process can either suppress or favor the EPB development, the latter case being usually accompanied by a significant uplift of the ionospheric plasma (e.g. Ossakow and Chaturvedi, 1978; Aarons, 1991; Abdu et al., 1995; Fejer et al., 1999; Basu et al., 2001, 2007). Recently, significant plasma bubbles have been observed also at mid latitudes. Specifically, Ma and Maruyama (2006) observed, for the first time, a super-bubble at mid latitudes over Japan during the moderate February 12, 2000 geomagnetic storm; Huang et al. (2007a) using data from the Defense Meteorological Satellite Program satellites for the 2003 Halloween super-storm, observed mid-latitude depletions and interpreted them as EPBs that almost reached the plasmapause; Cherniak and Zakharenkova (2016) found large-scale plasma bubbles extending toward Europe and induced by PPEFs generated by the June 2015 geomagnetic storm.

A better understanding of the generation mechanisms and dynamics of EPBs has become a priority for the space weather community, because they can severely affect trans-ionospheric radio waves and hence communication and navigation systems. Although EPBs have been extensively studied for several decades (Tsunoda, 1980, 2005; Zalesak and Ossakow, 1980; Farley et al., 1986; Fejer et al., 1999; Keskinen et al., 2003; Bhattacharyya, 2004; Otsuka et al., 2004; Bumrungkit et al., 2018; Joshi et al., 2019; Marew et al., 2019; Yokoyama, 2017; Wan et al., 2019), there are still some outstanding questions that need to be clarified to improve our current understanding of their seeding mechanisms. More specifically, an important issue to clarify is how magnetic storms affect the generation of EPBs.

In this paper, we present the analysis of a significant EPB detected by CSES-01 and Swarm satellite missions during the August 2018 geomagnetic storm. By using a multi-instrumental approach, we suggest that an impulsive variation of the solar wind (SW) pressure might be responsible for the formation of such irregularity. Section 2 describes the data used in the analysis, Section 3 illustrates and discusses the results, while the conclusions are the subject of Section 4.

2. Data source

CSES-01 is the first satellite, in orbit since February 2018, of the multi-satellite China Seismo-Electromagnetic Satellite (CSES) mission (Shen et al., 2018). It is a sun-synchronous satellite flying at an altitude of ~507 km; its orbital descending node time is at around 14:00 local time (LT), while the ascending one is at around 2:00 LT, the revisiting period being of about 5 days. CSES-01 hosts nine payloads: a high-precision magnetometer (HPM; Zhou et al., 2018), a search coil magnetometer (Wang Q. et al., 2018), an electric field detector (EFD; Huang et al., 2018), a Langmuir probe (LAP; Yan et al., 2018), a plasma analyzer (Liu et al., 2019), a high energetic particle package (Li et al., 2019), a high-energy particle detector (Picozza et al., 2019), a Global Navigation Satellite System occultation receiver (Lin et al., 2018), and a tri-band beacon (Chen et al., 2018).

HPM comprises a dual fluxgate magnetometer which can record the magnetic vector and intensity in the frequency range from Direct Current (DC) to 15 Hz. EFD measures the potential of four probes (floating potential, V_f hereafter), installed at the tips of the four booms, and derives the electric field as the difference among V_f in the frequency range between DC and 3.5 MHz (Huang et al., 2018). LAP is designed to measure in-situ plasma density and electron temperature every 3 s in survey mode and every 1.5 s in burst mode. In this study we used 1 s resolution geomagnetic field (from HPM), 1 s resolution electric field (from EFD) and 3 s resolution electron density (from LAP) data. To obtain reliable electric field observations, we removed from EFD data the $\mathbf{v}_s \times \mathbf{B}$ contribution due to satellite's motion, being $\mathbf{v}_s$ the velocity of the satellite and $\mathbf{B}$ the observed geomagnetic field. Both EFD and HPM data are given in a geographical coordinate frame.

Swarm is a constellation of three Low Earth Orbit satellites (named A, B, and C) launched at the end of 2013 by the European Space Agency (ESA) (Friis-Christensen et al., 2006, 2008). Swarm satellites are orbiting the Earth in a circular near-polar orbit; A and C fly side-by-side at the same altitude that was of about 440 km on August 2018 (with an inclination of 87.35°, an east–west separation of 1–1.5° in longitude, and a maximal differential delay in orbit of approximately 10 s), while B flies at an altitude that was of about 510 km in the same period (with an inclination of 87.75°) in an orbital plane which has gradually got farther away from those of the other two satellites during the mission's lifetime (9 LT hours after 4 years). All Swarm satellites are equipped with identical

instruments consisting of Global Positioning System receivers and sensors for measuring both magnetic and electric fields, and plasma density. In this work we used Level 1b electron density measurements with a resolution of 1 s (https://earth.esa.int/documents/10174/1514862/Swarm_L1b_Product_Definition) made by the Langmuir probe (LP) (Knudsen et al., 2017; Lomidze et al., 2018).

For solar wind parameters analysis, we used THEMIS-E satellite data, namely the moments of the ion distribution functions obtained from the on-board moments calculations of the electrostatic analyzer (McFadden et al., 2008), which operates in the range from 25 eV to 25 keV, and the magnetic field measurements of the fluxgate magnetometer (Auster et al., 2008) in the geocentric solar ecliptic system.

3. Results and discussion

On August 25, 2018 an interplanetary coronal mass ejection (ICME) arrived at the Earth at 13:55 universal time (UT), generating a G3-class geomagnetic storm. As shown by Piersanti et al. (2020), on August 26, 2018 at 7:11 UT, and as visible in Fig. 1, the SYM-H index fell down to −206 nT. Indeed, the north–south component B_z of the interplanetary magnetic field (IMF) recorded onboard ACE satellite at around 16:00 UT on August 25 switched southward for around eighteen hours, reaching a maximum negative value of ~−20 nT; then it turned northward for a very long recovery phase of about 5 days. Simultaneously, again starting at around 16:00 UT of August 25, solar wind pressure experiences a constant increase lasting about fourteen hours, while solar wind speed seems to maintain quite a stable value around 400 km/s.

Generally, when a sudden intensification of the westward ring current occurs, PPEFs from high latitudes trigger low-latitude ionospheric irregularities (Basu et al., 2001, 2005). Specifically, in the post-sunset zone, an eastward PPEF superimposes on the local eastward electric field due to the ionospheric dynamo, causing a fast uplift of the ionospheric plasma that may generate EPBs (Basu et al., 2007; Cherniak and Zakharenkova, 2016).

On August 26, 2018 between ~01:27 UT and ~01:31 UT, during the main phase of the geomagnetic storm, CSES-01 observed a significant EPB over the equatorial western African region (Fig. 2a, cyan part of the black orbit); specifically, the electron density measured by CSES-01 fell down from ~$5{\cdot}10^{10}$ m^{-3} to ~$4{\cdot}10^{7}$ m^{-3} (Fig. 2b, black curve). The same bubble is recorded by Swarm A between ~01:55 UT and ~02:05 UT (Fig. 2a, cyan part of the red orbit; Fig. 2b, red curve). It is worth mentioning that CSES-01 electron density (N_e) data were calibrated ($N_{e,cal}$) according to the following relation:

$$N_{e,cal} = N_e \cdot 1.35 \cdot 1.5, \quad (1)$$

where the multiplication factors 1.35 and 1.5 take into account, respectively, the Wipple effect (Whipple, 1990) and the different altitude between CSES-01 and Swarm A orbits. Fig. 2 shows that, even though the Swarm A LP saturates for electron density values by far higher than those saturating the CSES-01 LAP, the EPB latitudinal extension (~15–20°) is well defined by both satellites. The slight difference between the EPB latitudinal extension recorded by

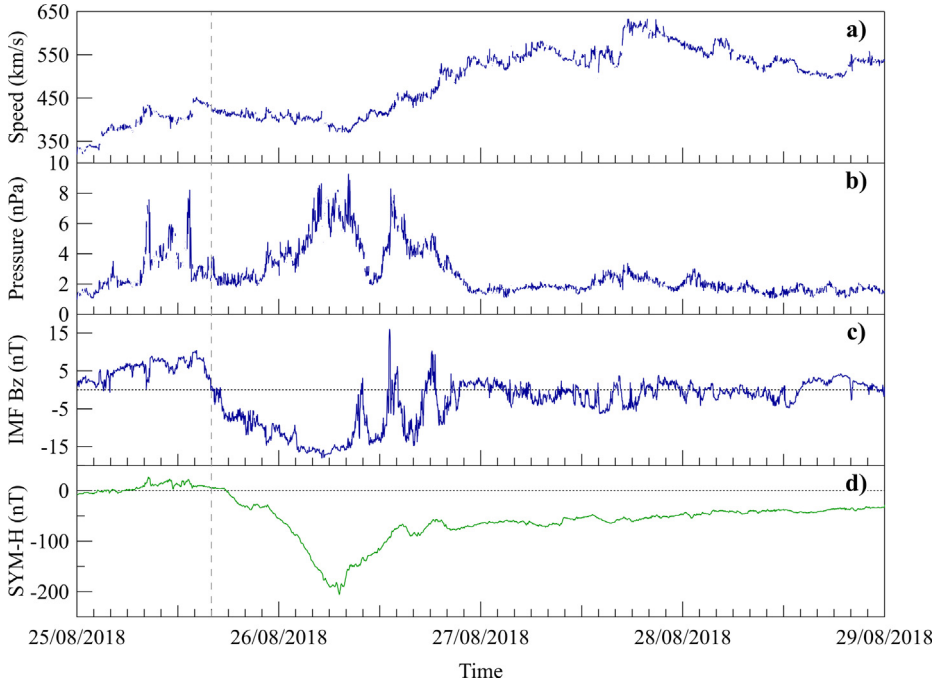

Fig. 1. ACE satellite solar wind parameters and IMF, and SYM-H index. From top to bottom: solar wind speed (a) and pressure (b), IMF B_z component (c), SYM-H index (d). The horizontal dotted black lines in panels c and d represent a zero line. The vertical dashed grey line indicates the 16:00 UT of August 25.

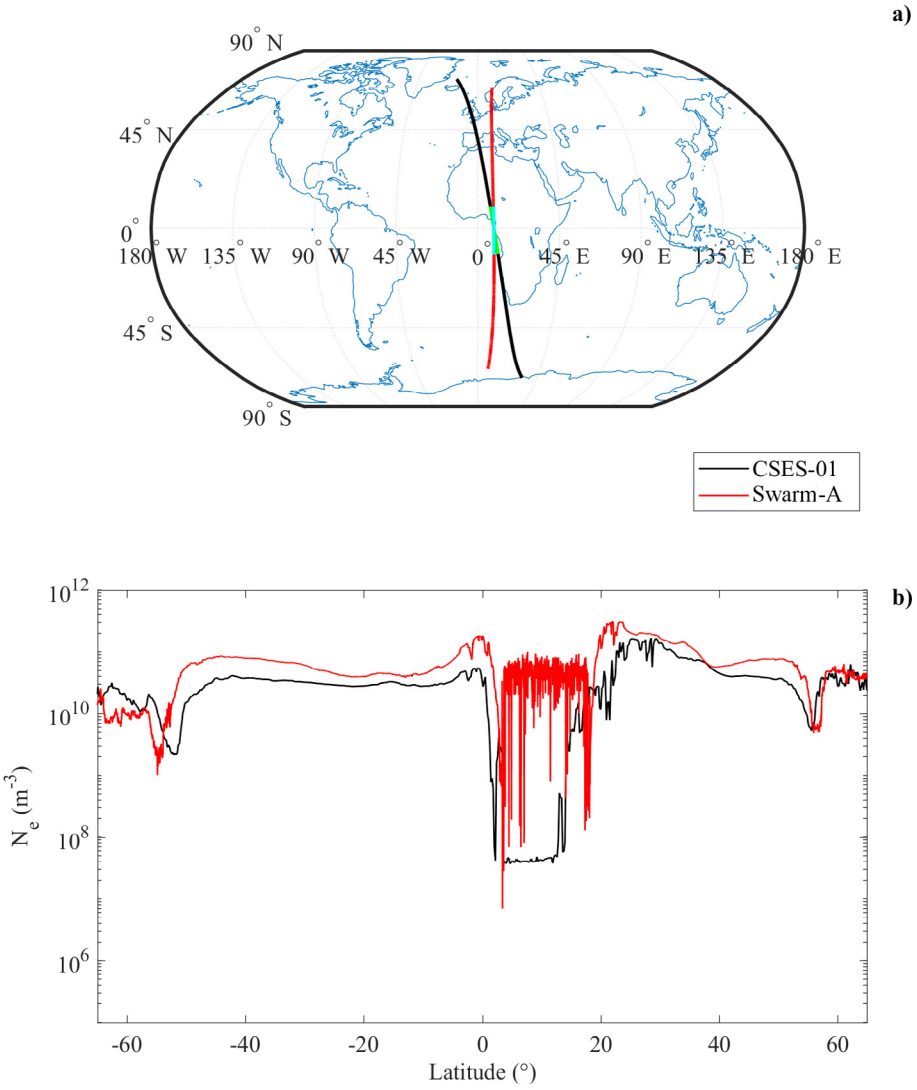

Fig. 2. Plasma bubble detection by CSES-01 and Swarm A satellites. (Panel a) CSES-01 orbit (black), between 01:15 UT and 01:45 UT, and Swarm A orbit (red), between 01:38 UT and 02:08 UT, on August 26, 2018; the cyan parts of both orbits highlight the time interval when the EPB was detected by each satellite. (Panel b) electron density as measured by (black) CSES-01 and (red) Swarm A. (For interpretation of the references to colour in this figure legend, the reader is referred to the web version of this article.)

CSES-01 and Swarm has to be simply ascribed to the evolution characterizing the bubble in the time interval differentiating the two orbits. At the same time, taking into account that the Swarm A orbit is about 30 min later than the CSES-01 one, we can claim that this structure is rather stable both in space and time.

This passage through the EPB is confirmed by the EFD observations as shown by Fig. 3, where the four measured probe potentials (V_A, V_B, V_C and V_D) and the components (E_X, E_Y, E_Z) of the electric field **E** are illustrated.

For each probe, V_f adjusts so that the sum of all the entering electric currents is equal to zero, i.e.:

$$\sum_j I_j = 0, \tag{2}$$

where I_j are the ion and electron currents collected by the plasma, the photoelectron emission and the bias current injected by the EFD electronics. Since the bias current is fixed at 500 nA and the photoelectron current is negligible, V_f can be considered linearly dependent on the plasma density variations (Diego et al., 2017). Concerning the really smoothed low values by CSES-01 in Fig. 2, the lowest value of electron density leading EFD to saturation can be estimated from the plasma current equation relative to the electron density (Boyd, 1968; Diego et al., 2017, and references therein), i.e.:

$$I_e = \frac{1}{4} q N_e \sqrt{\frac{8 k_B T_e}{\pi m_e}} S_e \left(1 + \frac{q \Delta V}{k_B T_e}\right), \tag{3}$$

where k_B is the Boltzmann constant, T_e is the electron temperature, m_e is the electron mass, S_e is the probe surface, q is the electric charge, ΔV is the difference between the local plasma potential and the probe potential, and N_e is the electron density. From Eq. (3) it can be computed that

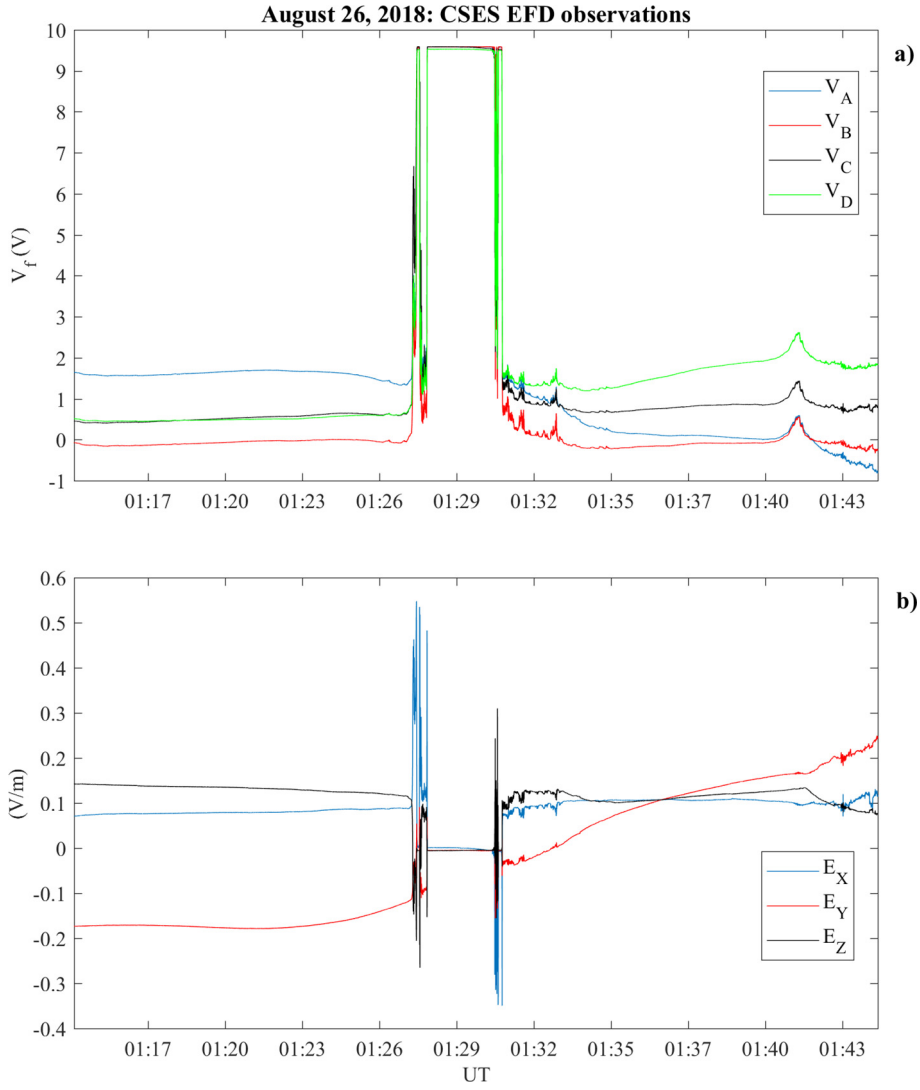

Fig. 3. CSES-01 EFD observations on August 26, 2018 between 01:15 UT and 01:45 UT: panel a) probe potentials V_A (blue), V_B (red), V_C (black) and V_D (green); panel b) electric field components E_X (blue), E_Y (red) and E_Z (black), derived by probe potentials, expressed in the geographical reference frame, where X is the North-South direction, Y is the East-West direction and Z is the local vertical direction. (For interpretation of the references to colour in this figure legend, the reader is referred to the web version of this article.)

saturation occurs only when $N_e < 7{\cdot}10^7\ m^{-3}$ (considering an average electron temperature of 2300 K). This highlights the higher capability of CSES-01 LAP to record this kind of deep electron density depletions with respect to Swarm LP.

In Fig. 3, the plateaus centered at around 01:29 UT are the clear signature of the EFD saturation that occurs when the satellite is inside the EPB. This is due to the EFD electronic design that allows a maximum V_f value of about 9.6 V. If the plasma density decreases, V_f moves naturally toward positive values to collect more electrons, thus satisfying Eq. (2). Each time that very low values of electron densities are experienced, the injected bias becomes dominant and V_f easily increases up to the saturation level.

Fig. 3 shows also significant fluctuations at both edges of the EPB. These have been interpreted by Pottelette et al. (2007) in terms of Kinetic Alfven waves.

The same fluctuations, observed when the satellite enters and exits from the EPB, are also shown in Fig. 4 where the values of v_z component of plasma drift velocity $\mathbf{v}$, evaluated as $\mathbf{v} = \left(\mathbf{E}\mathrm{x}\mathbf{B}/B^2\right)$ using both HPM and EFD data recorded by CSES-01, are plotted.

As highlighted before, during quiet conditions, EPBs are usually generated in the post-sunset sector due to the Rayleigh-Taylor instability linked to the ionospheric dynamo dynamics characterizing low latitudes, after which they drift eastward (e.g. Whalen, 2000). So, in the first instance one may think that the depletion shown in Fig. 2 is a "fossil" EPB, that is an EPB generated far away from the site, specifically in the post-sunset sector, which zonally drifted eastward (Saito and Maruyama, 2006; Sekar et al., 2007). At the same time, it is also true that, especially during disturbed conditions, EPBs can be generated also in LT sectors different from the post-sunset one,

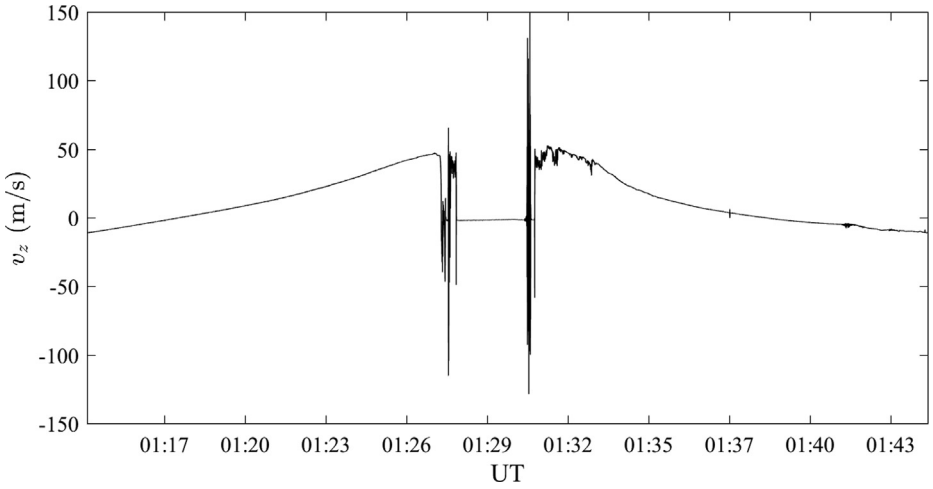

Fig. 4. v_z component of plasma drift velocity **v** recorded by CSES-01 when passing through the bubble in the geographical reference frame, evaluated as $\mathbf{v} = (\mathbf{E}\mathbf{x}\mathbf{B}/B^2)$, using both HPM and EFD data.

as shown by Wan et al. (2019) who performed a statistical study of equatorial plasma depletions occurrence considering a large dataset of 181 geomagnetic storms.

In order to investigate a possible connection between the solar wind dynamics and the appearance of the EPB shown in Fig. 2, we collected data from THEMIS-E that, in the period under investigation, was located in the interplanetary space, very close to the Earth's magnetosphere (red circle in Fig. 5). Specifically, we analyzed observations between 00:15 UT and 02:45 UT on August 26, 2018 (Fig. 5) of IMF magnitude (panel a), plasma density ρ (panel b) and dynamic pressure P (panel c), using data from the spacecraft-collected fluxgate magnetometer and from the on board electron/ion moments instrument.

Fig. 5 shows that between 00:15 UT and 01:05 UT THEMIS-E was in the interplanetary space, since it was measuring values of plasma density and magnetic field that are consistent with the SW observations at L1 point during the passage of the ICME (Piersanti et al., 2020). This is confirmed in Fig. 5d which shows THEMIS-E position at 01:00 UT with respect to the magnetopause as modeled by Shue et al. (1998) and to the bow shock as modeled by Farris and Russell (1994). Fig. 5d clearly shows that, at this time, the satellite was well outside the Earth's bow shock. It is only at about 02:00 UT that THEMIS-E came back inside the magnetosheath, as confirmed by the clear upstream wave activity before and after the sudden change of both plasma and magnetic field parameters (Bavassano et al., 1971; Lepidi et al., 1996; Turc et al., 2014).

However, between 01:06 UT and 01:11 UT, THEMIS-E detected a sudden change in both the magnetic field and plasma parameters (Fig. 5a–c). This indicates the crossing of the bow shock and the entrance in the magnetosheath, as confirmed by the values of both the magnetic field (~50 nT) and plasma density (~55 cm^{-3}) that are higher than their typical values (e.g. Merka et al., 2005; Turc et al., 2014; Wang J. et al., 2018). Successively, at 01:12 UT, THEMIS-E crossed again the bow shock, entering again the interplanetary space, as confirmed by the sudden decrease of both plasma parameters and magnetic field.

This behavior can be explained in terms of an impulsive variation (a sudden decrease followed by a really quick recovery) of the SW dynamic pressure during the ICME passage (Turc et al., 2014, and references therein) that led to an impulsive expansion and then contraction of the magnetosphere, lasting approximately 5 min.

By comparing the time at which the EPB is recorded by CSES-01 (Fig. 2b) to that of the SW structure detected by THEMIS-E, we find a delay time of $T_E = 21 \pm 1$ min, which is consistent with the transmission time of the interplanetary electric field to the equatorial ionosphere (Kelley et al., 1979; Huang et al., 2005; Wolf et al., 2007). Indeed, Bhaskar and Vichare (2013) showed that the delay time (T_D) between satellite observations in the interplanetary space and ground-based measurements can be expressed as:

$$T_D = T_A + T_{B,M} + T_{Alf} + T_T + T_R + T_{Trans}, \quad (4)$$

where T_A is the advection time of the SW to travel from the satellite to the Earth's bow shock, $T_{B,M}$ is the propagation time from the bow shock to the magnetopause, T_{Alf} is the travel time along the magnetic field lines from the magnetopause to the polar ionosphere, T_T is the time needed by the interplanetary electric field to cross the magnetosphere, T_R is the reconfiguration time of the magnetosphere-ionosphere system, and T_{Trans} is the propagation time from the high latitudes to the equatorial ionosphere.

If we apply Eq. (4) to THEMIS-E data, following the results obtained by Khan and Cowley (1999) for the east–west ionospheric flow on the nightside, and neglecting T_A (because of the THEMIS-E proximity to the Earth's bow shock), we obtain: $T_{B,M} = 0.9 \pm 0.5$ min; $T_{Alf} = 2.6 \pm 0.8$ min; $T_T = 1.6 \pm 0.5$ min; $T_R = 12.7 \pm 2.2$ min; $T_{Trans} = 2.4 \pm 0.8$ min. The obtained values are in agreement with the observations of Manoj et al. (2008). As a

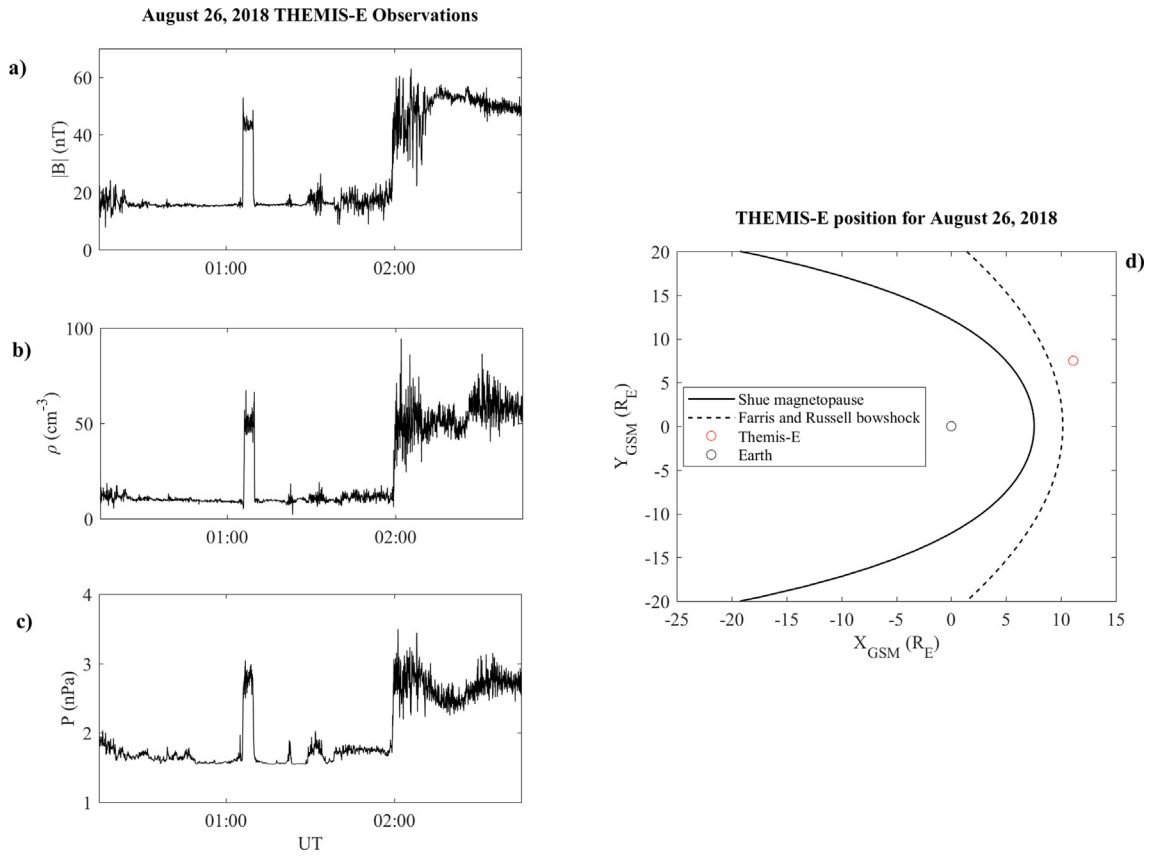

Fig. 5. THEMIS-E observations between 00:15 UT and 02:45 UT on August 26, 2018: panel a) IMF magnitude; panel b) SW plasma density ρ; panel c) SW dynamic pressure P. Panel d) shows the THEMIS-E position (red circle) at 01:00 UT in the ecliptic plane with respect to the magnetopause (black curve) as modeled by Shue et al. (1998) and to the bow shock (black dotted curve) as modeled by Farris and Russell (1994). All the observations are expressed in the geocentric solar magnetic system; R_E on the axes of panel d) stands for the Earth radius.

consequence, we found $T_D = 20.2 \pm 2.0$ min, which is consistent with the observed T_E.

This result suggests a possible link between the SW dynamic pressure impulsive variation identified by THEMIS-E and the generation of the EPB detected by CSES-01 and Swarm A. Specifically, such an impulsive variation of the SW parameters may have played a key role in generating this large EPB. In fact, the similarity between T_D and T_E leads us to think that the EPB detected by CSES-01 is not a "fossil" bubble generated in the post-sunset sector and then moved to the East, but rather a real "fresh" bubble generated right in that post-midnight sector. In support of this, the structure appears to be rather stable as Swarm A detected it in practically the same position about half an hour later, while considering a zonally drift velocity between 100 m/s and 200 m/s (Ji et al., 2015) it should have moved of about 200–400 km. Moreover, this fact is also supported by the following considerations: (1) well-developed plasma bubbles occur in the local midnight-dawn sector at low solar activity (in August 2018 the solar index R_{12} was equal to 6.7) (Huang et al., 2012), also during disturbed conditions (Wan et al., 2019); (2) several statistical studies (Stolle et al., 2006; Huang et al., 2014; Okoh et al., 2017) have shown that, in the African sector under investigation, the highest EPB occurrence is recorded during equinoxes, in a time window including the local time sector here investigated.

The idea is that this impulsive variation of the SW pressure triggered an eastward PPEF that propagated from high to equatorial latitudes. In the nightside region, this PPEF overlapped the local westward electric field (Balan and Bailey, 1995; Astafyeva et al., 2016), causing either a reduction or an inversion. In both cases the vertical ionospheric plasma drift was suddenly directed from downward to upward (Nicolls et al., 2006), which triggered most likely the observed EPB (Basu et al., 2007; Cherniak and Zakharenkova, 2016; Abdu, 2019).

On the other hand, an additional contribution to this uplift could be due also to the modification of the ionospheric dynamo. In fact, during quiet conditions, at night the ionospheric dynamo is such that the ionospheric plasma would move downward. However, during disturbed conditions, a geomagnetic storm induced energy input to the thermosphere may alter the global thermospheric circulation, with a consequent disturbance of the ionospheric dynamo which is at the base of a plasma uplift (Nicolls et al., 2006; Fejer et al., 2008). Indeed, Fejer et al. (2008) showed that, between approximately 00 LT and 06 LT

(i.e. a time window including the one here investigated), disturbance dynamo drifts are always upwards for disturbed conditions.

4. Conclusions

In this paper, data from CSES-01, Swarm A, and THEMIS-E are analyzed to investigate the possible origin of a significant post-midnight EPB occurred on August 26, 2018 over western Africa, during the main phase of a geomagnetic storm. Specifically, the analysis supports the hypothesis of a direct link between an impulsive variation of the SW dynamic pressure, observed by THEMIS-E, and the deep EPB observed by CSES-01 and Swarm A. Indeed, the delay time between the impulsive variation of the SW parameters and the detection of the ionospheric EPB very well matches with the theoretical delay time between satellite observations in the interplanetary space and ground-based measurements. A possible mechanism able to explain this link, and hence at the origin of the observed EPB, can be summarized in the following chain of events, temporally ordered from the first to the last:

1. impulsive variation of the SW pressure during the passage of the magnetic cloud;
2. generation of an eastward prompt penetrating electric field which propagates to the nightside equatorial ionosphere;
3. intensification of an upward disturbance dynamo drift;
4. occurrence of either a sudden decrease of the nightside westward equatorial electrojet or a reversal of it;
5. significant uplift of the ionospheric plasma which is at the base of the detected EPB, which is really a "fresh" EPB generated in the post-midnight sector.

Availability of data and materials

CSES-01 data are freely available at https://www.leos.ac.cn/. THEMIS-E data are freely available at https://cdaweb.sci.gsfc.nasa.gov/. Swarm data are freely available at http://earth.esa.int/swarm.

Declaration of Competing Interest

The authors declare that they have no known competing financial interests or personal relationships that could have appeared to influence the work reported in this paper.

Acknowledgements

The authors gratefully acknowledge Prof. Villante for his comments and suggestions regarding the THEMIS-E data. This work is in the framework of the CSES-Limadou Collaboration (http://cses.roma2.infn.it). This work made use of the data from CSES mission, a project funded by the China National Space Administration and the China Earthquake Administration in collaboration with the Italian Space Agency and the Istituto Nazionale di Fisica Nucleare; corresponding data are freely available at http://www.leos.ac.cn/. The authors thank the European Space Agency (ESA) for making Swarm data publicly available via ftp://swarmdiss.eo.esa.int, and for the considerable efforts made for the Langmuir probes data calibration. The THEMIS program was supported by NASA under contract NAS5-02099. The authors kindly acknowledge N. Papitashvili and J. King at the National Space Science Data Center of the Goddard Space Flight Center for the use permission of both THEMIS-E and OMNI data and the NASA CDAWeb team for making these data available. M. Piersanti thanks the Italian Space Agency for the financial support under the contract ASI "LIMADOU scienza" n° 2016-16-H0. This research was supported by the Italian MIUR-PRIN on "Circumterrestrial environment: impact of Sun – Earth Interaction" and by the ISSI-BJ project "The electromagnetic data validation and scientific application research based on CSES satellite".

References

Aarons, J., 1991. The role of the ring current in the generation or inhibition of equatorial F-layer irregularities during magnetic storms. Radio Sci. 26, 1131–1149. https://doi.org/10.1029/91RS00473.

Abdu, M.A., 2019. Day-to-day and short-term variabilities in the equatorial plasma bubble/spread F irregularity seeding and development. Progress Earth Plan. Sci. 6, 11. https://doi.org/10.1186/s40645-019-0258-1.

Abdu, M.A., Batista, I.S., Walker, G.O., Sobral, J.H.A., Trivedi, N.B., de Paula, E.R., 1995. Equatorial ionospheric fields during magnetospheric disturbances: Local time/longitudinal dependences from recent EITS campaigns. J. Atmos. Sol. Terr. Phys. 57, 1065–1083. https://doi.org/10.1016/0021-9169(94)00123-6.

Astafyeva, E., Zakharenkova, I., Alken, P., 2016. Prompt penetration electric fields and the extreme topside ionospheric response to the June 22–23, 2015, geomagnetic storms as seen by the Swarm constellation. Earth Planets Space 68, 152. https://doi.org/10.1186/s40623-016-0526-x.

Auster, H.U., Glassmeier, K.H., Magnes, W., Aydogar, O., Baumjohann, W., Constantinescu, D., Fischer, D., Fornacon, K.H., Georgescu, E., Harvey, P., Hillenmaier, O., Kroth, R., Ludlam, M., Narita, Y., Nakamura, R., Okrafka, K., Plaschke, F., Richter, I., Schwarzl, H., Stoll, B., Valavanoglou, A., Wiedemann, M., 2008. The THEMIS fluxgate magnetometer. Space Sci. Rev. 141, 235–264. https://doi.org/10.1007/978-0-387-89820-9_11.

Balan, N., Bailey, G.J., 1995. Equatorial plasma fountain and its effect: possibility of an additional layer. J. Geophys. Res. 100, 21421–21432. https://doi.org/10.1029/95JA01555.

Basu, S., Basu, S., Groves, K.M., Yeh, H., Su, S., Rich, F.J., Sultan, P.J., Keskinen, M.J., 2001. Response of the equatorial ionosphere in the South Atlantic region to the great magnetic storm of July 15, 2000. Geophys. Res. Lett. 28, 3577–3580. https://doi.org/10.1029/2001GL013259.

Basu, S., Basu, S., Groves, K.M., Mackenzie, E., Keskinen, M.J., Rich, F. J., 2005. Near-simultaneous plasma structuring in the midlatitude and equatorial ionosphere during magnetic superstorms. Geophys. Res. Lett. 32, L12S05. https://doi.org/10.1029/2004GL021678.

Basu, S., Rich, F.J., Groves, K.M., MacKenzie, E., Coker, C., Sahai, Y., Fagundes, P.R., Becker-Guedes, F., 2007. Response of the equatorial ionosphere at dusk to penetration electric fields during intense magnetic storms. J. Geophys. Res. 112, A08308. https://doi.org/10.1029/2006JA012192.

Bhattacharyya, A., 2004. Role of E region conductivity in the development of equatorial ionospheric plasma bubbles. Geophys. Res. Lett. 31, L06806. https://doi.org/10.1029/2003GL018960.

Bavassano, B., Mariani, F., Villante, U., Ness, N.F., 1971. Multiple crossings of the Earth's bow shock at large geocentric distances. J. Geophys. Res. 76 (25), 5970–5977. https://doi.org/10.1029/JA076i025p05970.

Bhaskar, A., Vichare, G., 2013. Characteristics of penetration electric fields to the equatorial ionosphere during southward and northward IMF turnings. J. Geophys. Res. 118, 4696–4709. https://doi.org/10.1002/jgra.50436.

Blanc, M., Richmond, A.D., 1980. The ionospheric dynamo. J. Geophys. Res. 85, 1669–1686. https://doi.org/10.1029/JA085iA04p01669.

Boyd, R.L.F., 1968. Langmuir probes on spacecraft. In: Lochte-Holtgreven, W. (Ed.), Plasma Diagnostics. North Holland, Amsterdam, Netherlands.

Bumrungkit, A., Supnithi, P., Saito, S., 2018. Statistical analysis of separation distance between equatorial plasma bubbles near Suvarnabhumi International Airport, Thailand. J. Geophys. Res. 123. https://doi.org/10.1029/2018JA025612.

Chen, L., Ou, M., Yuan, Y.P., Sun, F., Yu, X., Zhen, W.M., 2018. Preliminary observation results of the Coherent Beacon System onboard the China Seismo-Electromagnetic Satellite-1. Earth. Plan. Phys. 2 (6), 505–514. https://doi.org/10.26464/epp2018049.

Cherniak, I., Zakharenkova, I., 2016. First observations of super plasma bubbles in Europe. Geophys. Res. Lett. 43, 11137–11145. https://doi.org/10.1002/2016GL071421.

Diego, P., Bertello, I., Candidi, M., Mura, A., Vannaroni, G., Badoni, D., 2017. Plasma and fields evaluation at the Chinese seismo-electromagnetic satellite for electric field detector measurements. IEEE Access. 5, 3824–3833. https://doi.org/10.1109/ACCESS.2017.2674019.

Farley, D.T., Balsley, B.B., Woodman, R.F., Mc-Clure, J.P., 1970. Equatorial spread-F: Implications of VHF radar observations. J. Geophys. Res. 75 (34), 7199–7216. https://doi.org/10.1029/JA075i034p07199.

Farley, D.T., Bonelli, E., Fejer, B.G., Larsen, M.F., 1986. The prereversal enhancement of the zonal electric field in the equatorial ionosphere. J. Geophys. Res. 91, 13723–13728. https://doi.org/10.1029/JA091iA12p13723.

Farris, M.H., Russell, C.T., 1994. Determining the standoff distance of the bow shock: Mach number dependence and use of models. J. Geophys. Res. 99, 17681. https://doi.org/10.1029/94JA01020.

Fejer, B.G., Jensen, J.W., Su, S.-Y., 2008. Seasonal and longitudinal dependence of equatorial disturbance vertical plasma drifts. Geophys. Res. Lett. 35, L20106. https://doi.org/10.1029/2008GL035584.

Fejer, B.G., Scherliess, L., 1995. Time dependent response of equatorial ionospheric electric field to magnetospheric disturbances. Geophys. Res. Lett. 22, 851–854. https://doi.org/10.1029/95GL00390.

Fejer, B.G., Scherliess, L., de Paula, E.R., 1999. Effects of the vertical plasma drift velocity on the generation and evolution of equatorial spread F. J. Geophys. Res. 104, 19859–19869. https://doi.org/10.1029/1999JA900271.

Friis-Christensen, E., Lühr, H., Hulot, G., 2006. Swarm: A constellation to study the Earth's magnetic field. Earth Plan. Space 58, 351–358. https://doi.org/10.1186/BF03351933.

Friis-Christensen, E., Lühr, H., Knudsen, D., Haagmans, R., 2008. Swarm – An Earth observation mission investigating geospace. Adv. Space Res. 41, 210–216. https://doi.org/10.1016/j.asr.2006.10.008.

Huang, C., Foster, J.C., Kelley, M.C., 2005. Long-duration penetration of the interplanetary electric field to the low-latitude ionosphere during the main phase of magnetic storms. J. Geophys. Res. 110, A11309. https://doi.org/10.1029/2005JA011202.

Huang, C.-S., de La Beaujardiere, O., Roddy, P.A., Hunton, D.E., Ballenthin, J.O., Hairston, M.R., 2012. Generation and characteristics of equatorial plasma bubbles detected by the C/NOFS satellite near the sunset terminator. J. Geophys. Res. 117, A11313. https://doi.org/10.1029/2012JA018163.

Huang, C.-S., de La Beaujardiere, O., Roddy, P.A., Hunton, D.E., Liu, J. Y., Chen, S.P., 2014. Occurrence probability and amplitude of equatorial ionospheric irregularities associated with plasma bubbles during low and moderate solar activities (2008–2012). J. Geophys. Res. Space Phys. 119, 1186–1199. https://doi.org/10.1002/2013JA019212.

Huang, C.-S., Foster, J.C., Sahai, Y., 2007a. Significant depletions of the ionospheric plasma density at middle latitudes: A possible signature of equatorial spread F bubbles near the plasmapause. J. Geophys. Res. 112, A05315. https://doi.org/10.1029/2007JA012307.

Huang, C.-S., Sazykinb, S., Chauc, J.L., Maruyamad, N., Kelley, M.C., 2007b. Penetration electric fields: Efficiency and characteristic time scale. J. Atmos. Terr. Phys. 69, 1135–1146. https://doi.org/10.1016/j.jastp.2006.08.016.

Huang, J.P., Lei, J.G., Li, S.X., Zeren, Z.M., Li, C., Zhu, X.H., Yu, W.H., 2018. The Electric Field Detector (EFD) onboard the ZH-1 satellite and first observational results. Earth Plan. Phys. 2 (6), 469–478. https://doi.org/10.26464/epp2018045.

Ji, S., Chen, W., Weng, D., Wang, Z., 2015. Characteristics of equatorial plasma bubble zonal drift velocity and tilt based on Hong Kong GPS CORS network: From 2001 to 2012. J. Geophys. Res. Space Phys. 120, 7021–7029. https://doi.org/10.1002/2015JA021493-T.

Joshi, L.M., Tsai, L.-C., Su, S.-Y., Otsuka, Y., Yokoyama, T., Yamamoto, M., Sarkhel, S., Hozumi, K., Lu, C.-H., 2019. Investigation of spatiotemporal morphology of plasma bubbles based on EAR observations. J. Geophys. Res. 124. https://doi.org/10.1029/2019JA026839.

Khan, H., Cowley, S.W.H., 1999. Observations of the response time of high-latitude ionospheric convection to variations in the interplanetary magnetic field using EISCAT and IMP-8 data. Ann. Geophys. 17, 1306–1335. https://doi.org/10.1007/s00585-999-1306-8.

Kelley, M.C., Fejer, B.G., Gonzales, C.A., 1979. An explanation for anomalous equatorial ionospheric electric fields associated with a northward turning of the interplanetary magnetic field. Geophys. Res. Lett. 6, 301–304. https://doi.org/10.1029/GL006i004p00301.

Keskinen, M.J., Ossakow, S.L., Fejer, B.G., 2003. Three-dimensional nonlinear evolution of equatorial ionospheric spread-F bubbles. Geophys. Res. Lett. 30 (16), 1855. https://doi.org/10.1029/2003GL017418.

Knudsen, D.J., Burchill, J.K., Buchert, S.C., Eriksson, A.I., Rida, G., Wahlund, J.-E., Ahlen, L., Smith, M., Moffat, B., 2017. Thermal ion imagers and Langmuir probes in the Swarm electric field instruments. J. Geophys. Res. 122, 2655–2673. https://doi.org/10.1002/2016JA022571.

Lepidi, S., Villante, U., Lazarus, A.J., Szabo, A., Paularena, K., 1996. Observations of bow shock motion during times of variable solar wind conditions. J. Geophys. Res. 101 (A5), 11107–11123. https://doi.org/10.1029/96JA00478.

Li, X.Q., Xu, Y.B., An, Z.H., Liang, X., Wang, P., Zhao, X.Y., Wang, H. Y., Lu, H., Ma, Y.Q., Shen, X.H., Wen, X.Y., Wang, H., Zhang, D.L., Shi, F., Peng, W.X., Gao, M., Yu, X.X., Wang, J.Z., Zhang, Y.J., Zhang, J.L., Zhang, J., Li, X., Zeng, J.R., Nan, Y.F., 2019. The high-energy particle package onboard CSES. Radiat. Detect. Technol. Methods 3, 22. https://doi.org/10.1007/s41605-019-0101-7.

Lin, J., Shen, X.H., Hu, L.C., Wang, L.W., Zhu, F.Y., 2018. CSES GNSS ionospheric inversion technique, validation and error analysis. Sci. China Tech. Sci. 61 (5), 669–677. https://doi.org/10.1007/s11431-018-9245-6.

Liu, C., Guan, Y., Zheng, X., Zhang, A., Piero, D., Sun, Y., 2019. The technology of space plasma in-situ measurement on the china seismo-electromagnetic satellite. Sci. China Tech. Sci. 62 (5), 829–838. https://doi.org/10.1007/s11431-018-9345-8.

Lomidze, L., Knudsen, D.J., Burchill, J., Kouznetsov, A., Buchert, S.C., 2018. Calibration and validation of Swarm plasma densities and electron temperatures using ground-based radars and satellite radio occultation measurements. Radio Sci. 53, 15–36. https://doi.org/10.1002/2017RS006415.

Ma, G., Maruyama, T., 2006. A super bubble detected by dense GPS network at East Asian longitude. Geophys. Res. Lett. 33, L21103. https://doi.org/10.1029/2006GL027512.

Manoj, C., Maus, S., Luhr, H., Alken, P., 2008. Penetration characteristics of the interplanetary electric field to the daytime equatorial

ionosphere. J. Geophys. Res. 113, A12310. https://doi.org/10.1029/2008JA013381.

Marew, H., Nigussie, M., Hui, D., Damitie, B., 2019. A method of estimating equatorial plasma vertical drift velocity and its evaluation using C/NOFS observations. Radio Sci. 54, 590–601. https://doi.org/10.1029/2019RS006800.

McFadden, J.P., Carlson, C.W., Larson, D., Ludlam, M., Abiad, R., Elliott, B., Turin, P., Marckwordt, M., Angelopoulos, V., 2008. The THEMIS ESA plasma instrument and in-flight calibration. Space Sci. Rev. 141, 277–302. https://doi.org/10.1007/978-0-387-89820-9_13.

Merka, J., Szabo, A., Slavin, J.A., Peredo, M., 2005. Three-dimensional position and shape of the bow shock and their variation with upstream Mach numbers and interplanetary magnetic field orientation. J. Geophys. Res. 110, 4202. https://doi.org/10.1029/2004JA010944.

Nicolls, M.J., Kelley, M.C., Vlasov, M.N., Sahai, Y., Chau, J.L., Hysell, D.L., Fagundes, P.R., Becker-Guedes, F., Lima, W.L.C., 2006. Observations and modeling of postmidnight uplifts near the magnetic equator. Ann. Geophys. 24, 1317–1331. https://doi.org/10.5194/angeo-24-1317-2006.

Okoh, D., Rabiu, B., Shiokawa, K., Otsuka, Y., Segun, B., Falayi, E., Onwuneme, S., Kaka, R., 2017. First study on the occurrence frequency of equatorial plasma bubbles over West Africa using an all-sky airglow imager and GNSS receivers. J. Geophys. Res. Space Phys. 122, 12430–12444. https://doi.org/10.1002/2017JA024602.

Ossakow, S.L., Chaturvedi, P.K., 1978. Morphological studies of rising equatorial spread F bubbles. J. Geophys. Res. 83 (A5), 2085–2090. https://doi.org/10.1029/JA083iA05p02085.

Otsuka, Y., Shiokawa, K., Ogawa, T., Yokoyama, T., Yamamoto, M., Fukao, S., 2004. Spatial relationship of equatorial plasma bubbles and field-aligned irregularities observed with an all-sky airglow imager and the equatorial atmosphere radar. Geophys. Res. Lett. 31, L20802. https://doi.org/10.1029/2004GL020869.

Picozza, P., Battiston, R., Ambrosi, G., Bartocci, S., Basara, L., Burger, W.J., Campana, D., Carfora, L., Casolino, M., Castellini, G., Cipollone, P., Conti, L., Contin, A., De Donato, C., De Santis, C., Follega, F.M., Guandalini, C., Ionica, M., Iuppa, R., Laurenti, G., Lazzizzera, I., Lolli, M., Manea, C., Marcelli, L., Martucci, M., Masciantonio, G., Mergè, M., Osteria, G., Pacini, L., Palma, F., Palmonari, F., Panico, B., Parmentier, A., Patrizi, L., Perfetto, F., Piersanti, M., Pozzato, M., Puel, M., Rashevskaya, I., Ricci, E., Ricci, M., Ricciarini, S., Scotti, V., Sotgiu, A., Sparvoli, R., Spataro, B., Vitale, V., Zuccon, P., Zoffoli, S., 2019. Scientific goals and in-orbit performance of the high-energy particle detector on board. Ap. J. Supp. Ser. 243 (1). https://doi.org/10.3847/1538-4365/ab276c.

Piersanti, M., Alberti, T., Bemporad, A., Berrilli, F., Bruno, R., Capparelli, V., Carbone, V., Cesaroni, C., Consolini, G., Cristaldi, A., Del Corpo, A., Del Moro, D., Di Matteo, S., Ermolli, I., Fineschi, S., Giannattasio, F., Giorgi, F., Giovannelli, L., Guglielmino, S.L., Laurenza, M., Lepreti, F., Marcucci, M.F., Martucci, M., Mergè, M., Pezzopane, M., Pietropaolo, E., Romano, P., Sparvoli, R., Spogli, L., Stangalini, M., Vecchio, A., Vellante, M., Villante, U., Zuccarello, F., Heilig, B., Reda, J., Lichtenberger, J., 2017. Comprehensive analysis of the geoeffective solar event of 21 June 2015: Effects on the magnetosphere, plasmasphere, and ionosphere systems. Sol. Phys. 292 (11), 169. https://doi.org/10.1007/s11207-017-1186-0.

Piersanti, M., De Michelis, P., Del Moro, D., Tozzi, R., Pezzopane, M., Consolini, G., Marcucci, M.F., Laurenza, M., Di Matteo, S., Pignalberi, A., Quattrociocchi, V., Diego, P., 2020. From the Sun to the Earth: August 25, 2018 geomagnetic storm effects. Ann. Geophys. 38, 703–724. https://doi.org/10.5194/angeo-38-703-2020.

Pottelette, R., Malingre, M., Berthelier, J.J., Seran, E., Parrot, M., 2007. Filamentary Alfvenic structures excited at the edges of equatorial plasma bubbles. Ann. Geophys. 25, 2159–2167. https://doi.org/10.5194/angeo-25-2159-2007.

Retterer, J.M., Roddy, P., 2014. Faith in a seed: On the origins of equatorial plasma bubbles. Ann. Geophys. 32, 485–498. https://doi.org/10.5194/angeo-32-485-2014.

Saito, S., Maruyama, T., 2006. Ionospheric height variations observed by ionosondes along magnetic meridian and plasma bubble onsets. Ann. Geophys. 24, 2991–2996. https://doi.org/10.5194/angeo-24-2991-2006.

Sekar, R., Chakrabarty, D., Sarkhel, S., Patra, A.K., Devasia, C.V., Kelley, M.C., 2007. Identification of active fossil bubbles based on coordinated VHF radar and airglow measurements. Ann. Geophys. 25, 2099–2102. https://doi.org/10.5194/angeo-25-2099-2007.

Shen, X.H., Zhang, X.M., Yuan, S.G., Wang, L.W., Cao, J.B., Huang, J. P., Zhu, X.H., Piergiorgio, P., Dai, J.P., 2018. The state-of-the-art of the China Seismo-Electromagnetic Satellite mission. Sci. China Tech. Sci. 61 (5), 634–642. https://doi.org/10.1007/s11431-018-9242-0.

Shue, J.-H., Song, P., Russell, C.T., Steinberg, J.T., Chao, J.K., Zastenker, G., Vaisberg, O.L., Kokubun, S., Singer, H.J., Detman, T.R., Kawano, H., 1998. Magnetopause location under extreme solar wind conditions. J. Geophys. Res. 103 (A8), 17691. https://doi.org/10.1029/98JA01103.

Stolle, C., Lühr, H., Rother, M., Balasis, G., 2006. Magnetic signatures of equatorial spread F as observed by the CHAMP satellite. J. Geophys. Res. 111, A02304. https://doi.org/10.1029/2005JA011184.

Tsunoda, R.T., 1980. Magnetic-field-aligned characteristics of plasma bubbles in the nighttime equatorial ionosphere. J. Atmos. Terr. Phys. 42, 743–752. https://doi.org/10.1016/0021-9169(80)90057-4.

Tsunoda, R.T., Livingston, R.C., McClure, J.P., Hanson, W.B., 1982. Equatorial plasma bubbles: Vertically elongated wedges from the bottomside F layer. J. Geophys. Res. 87, 9171–9180. https://doi.org/10.1029/JA087iA11p09171.

Tsunoda, R.T., 2005. On the enigma of day-to-day variability in equatorial spread F. Geophys. Res. Lett. 32, L08103. https://doi.org/10.1029/2005GL022512.

Turc, L., Fontaine, D., Savoini, P., Kilpua, E.K.J., 2014. Magnetic clouds' structure in the magnetosheath as observed by Cluster and Geotail: four case studies. Ann. Geophys. 32, 1247–1261. https://doi.org/10.5194/angeo-32-1247-2014.

Wan, X., Xiong, C., Wang, H., Zhang, K., Zheng, Z., He, Y., Yu, L., 2019. A statistical study on the climatology of the Equatorial Plasma Depletions occurrence at topside ionosphere during geomagnetic disturbed periods. J. Geophys. Res. 124. https://doi.org/10.1029/2019JA026926.

Wang, J., Guo, Z., Ge, Y.S., Du, A., Huang, C., Qin, P., 2018a. The responses of the earth's magnetopause and bow shock to the IMF Bz and the solar wind dynamic pressure: a parametric study using the AMR-CESE-MHD model. J. Space Weather Space Clim. 8 (A41). https://doi.org/10.1051/swsc/2018030.

Wang, Q., Huang, J.P., Zhang, X.M., Shen, X.H., Yuan, S.G., Zeng, L., Cao, J.B., 2018b. China seismo-electromagnetic satellite search coil magnetometer data and initial results. Earth Plan. Phys. 2 (6), 462–468. https://doi.org/10.26464/epp2018044.

Whalen, J.A., 2000. An equatorial bubble: Its evolution observed in relation to bottomside spread F and to the Appleton anomaly. J. Geophys. Res. 105, 5303–5315. https://doi.org/10.1029/1999JA900441.

Whipple, E.C., 1990. In: Singh, N., Wright, K.H, Jr., Stone, N.H. (Eds.), Current Collection from Space Plasmas. NASA CP-3089, 357 pp.

Wolf, R.A., Spiro, R.W., Sazykin, S., Toffoletto, F.R., 2007. How the Earth's inner magnetosphere works: An evolving picture. J. Atmos. Sol. Terr. Phys. 69, 288–302. https://doi.org/10.1016/j.jastp.2006.07.026.

Woodman, R.F., 1970. Vertical drift velocities and east-west electric fields at the magnetic equator. J. Geophys. Res. 75 (31), 6249–6259. https://doi.org/10.1029/JA075i031p06249.

Woodman, R.F., La Hoz, C., 1976. Radar observations of F region equatorial irregularities. J. Geophys. Res. 81 (31), 5447–5466. https://doi.org/10.1029/JA081i031p05447.

Yan, R., Guan, Y.B., Shen, X.H., Huang, J.P., Zhang, X.M., Liu, C., Liu, D.P., 2018. The Langmuir Probe onboard CSES: Data inversion analysis method and first results. Earth Plan. Phys. 2 (6), 479–488. https://doi.org/10.26464/epp2018046.

Yokoyama, T.A., 2017. Review on the numerical simulation of equatorial plasma bubbles toward scintillation evaluation and forecasting. Prog. Earth Planet. Sci. 4, 37. https://doi.org/10.1186/s40645-017-0153-6.

Zalesak, S.T., Ossakow, S.L., 1980. Nonlinear equatorial spread F: spatially large bubbles resulting from large horizontal scale initial perturbations. J. Geophys. Res. 85, 2131. https://doi.org/10.1029/JA085iA05p02131.

Zhou, B., Yang, Y.Y., Zhang, Y.T., Gou, X.C., Cheng, B.J., Wang, J.D., Li, L., 2018. Magnetic field data processing methods of the China Seismo-Electromagnetic Satellite. Earth Plan. Phys. 2 (6), 455–461. https://doi.org/10.26464/epp2018043.